Sensors **2007**, *7*, 2430-2445

sensors

ISSN 1424-8220

www.mdpi.org/sensors

Full Research Paper

Planar Array Sensor for High-speed Component Distribution Imaging in Fluid Flow Applications

Marco Jose da Silva*, Tobias Sühnel, Eckhard Schleicher, Roman Vaibar, Dirk Lucas and Uwe Hampel

Forschungszentrum Dresden-Rossendorf e.V., Institute of Safety Research, PO Box 510119, D-01314 Dresden, Germany

* Author to whom correspondence should be addressed. E-mail: m.dasilva@fzd.de

Received: 30 August 2007 / Accepted:17 October 2007 / Published: 19 October 2007

Abstract: A novel planar array sensor based on electrical conductivity measurements is presented which may be applied to visualize surface fluid distributions. The sensor is manufactured using printed-circuit board fabrication technology and comprises of 64 x 64 interdigital sensing structures. An associated electronics measures the electrical conductivity of the fluid over each individual sensing structure in a multiplexed manner by applying a bipolar excitation voltage and by measuring the electrical current flowing from a driver electrode to a sensing electrode. After interrogating all sensing structures, a two-dimensional image of the conductivity distribution over a surface is obtained which in turn represents fluid distributions over sensor's surface. The employed electronics can acquire up to 2500 frames per second thus being able to monitor fast transient phenomena. The system has been evaluated regarding measurement accuracy and depth sensitivity. Furthermore, the application of the sensor in the investigation of two different flow applications is presented.

Keywords: planar sensor, interdigital electrode, flow imaging, multiphase flow, multicomponent flow, phase distribution.

1. Introduction

Interdigital electrode structures have been used for decades in a large diversity of sensing applications and research fields. Among them the most common are nondestructive testing, chemical

and physical sensing, biotechnology and telecommunications [1-2]. The working principle of such interdigital sensors is based on the interaction of the electrical field generated by the sensor with the material or substance under test. The perturbation of the electrical field can be detected at a sensing electrode and is related to conductive or dielectric properties of the substance/material in the vicinity of the sensor. An important advantage of such electrode systems is the simple and cheap fabrication process and the possibility of investigation of materials or substances from measurements with a single side surface contact [1]. Most of the current technical implementations use one or a few sensing structures to investigate some material under test. In such cases the measurement accuracy must be high in order to assess chemical or physical material properties whereas the measuring time is normally not a concern and typically ranges from a few hundred of milliseconds to a few minutes depending on application and accuracy needs [1,3]. More recently multichannel sensors have been introduced to improve the capability of sensing systems [4]. This way, either the simultaneous measurement of multiple parameters [5] or the introduction of imaging capability has been achieved [6,7].

The characteristics described above make interdigital sensors very attractive to be employed in the investigation of flow phenomena. The high-speed measurement of fluid flow phenomena is of great interest in many industrial areas, e.g. in chemical and mechanical engineering, as well as in basic flow research, where the better understanding of such flows is required to improve efficiency and safety issues of plants and processes as well as for computational fluid dynamics (CFD) code development. For the investigation of highly transient multiphase and multicomponent flows we developed a novel high-speed imaging system based on the conductivity measurements of a multichannel interdigital sensor. The sensor comprises of 4096 interdigital sensing structures which are individually measured in a multiplexed manner. The conductivity measurement allows distinguishing a conducting from a non-conducting phase (e.g. water and gas) or the assessment of the component concentration in a two component mixing. This way, the images obtained from the sensor represent the component or phase distribution over the sensing area.

2. System design

The developed measuring system basically consists of a planar array sensor, a measuring electronics and a computer. The focus in implementing the system was the use of a multiplexed excitation scheme to reduce the number of connections to the sensor and a fast time response in the conductivity measurement to allow high-speed imaging.

2.1. Interdigital array sensor

The array sensor has been manufactured using standard printed-circuit board (PCB) fabrication technology and has 4096 interdigital sensing structures, which are multiplexed in a matrix with 64 driver (rows) and 64 sensing electrodes (column). Figure 1 presents the surface sensor and in detail the sensing structure, which has dimensions of 5.8 mm × 6.6 mm. The so called spatial wavelength of an interdigital structure is defined as the distance between the centerlines of neighboring electrodes of the same type (e.g., driving or sensing electrodes) and is of 2.6 mm for the developed sensor. The depth of penetration of the electric field generated by an interdigital sensor into the material is proportional to

the spatial wavelength [8]. Furthermore, the electrodes are gold plated to reduce electrochemical effects during the conductivity measurement. The sensor board was designed to fit to an experimental flow channel. The size of the whole sensor is 620 mm × 500 mm. Four connectors at the back side of the sensor (not shown in fig. 1) allow the sensor to be connected to the measuring electronics.

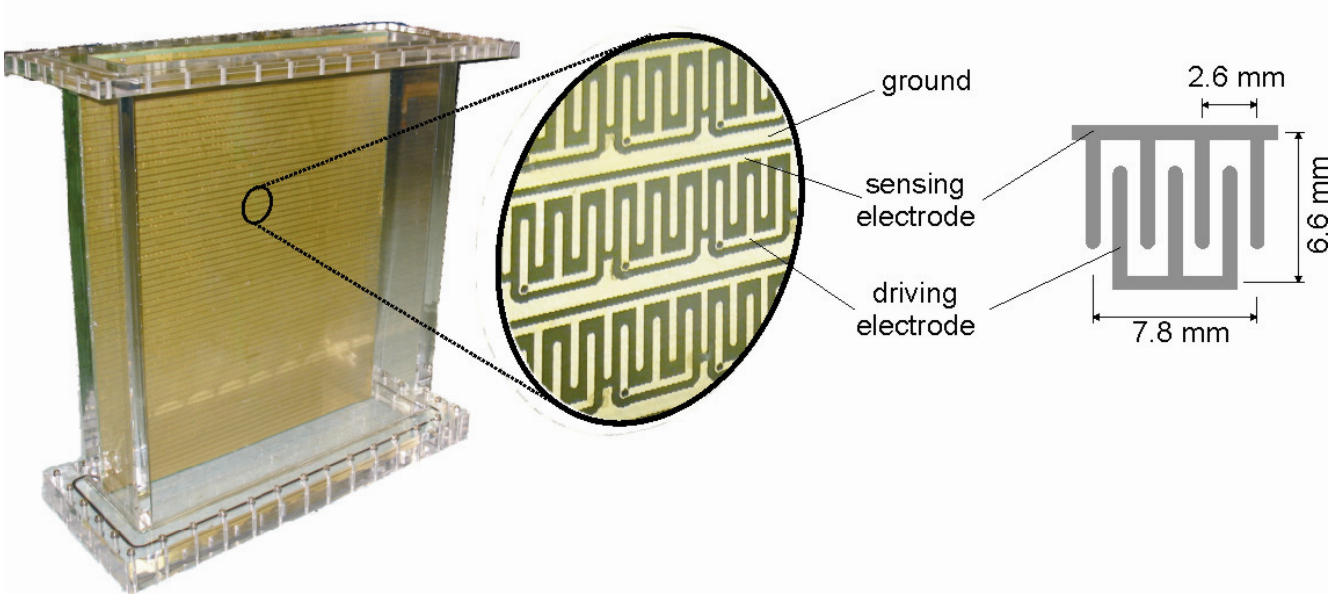

Figure 1. Printed circuit board surface sensor containing 64 × 64 interdigital sensing structures fitted to an experimental flow channel. The size of each sensing structure is 5.8 mm × 6.6 mm and the size of the whole sensor is 620 mm × 500 mm.

2.2. Measuring electronics

The measuring electronics applied for the conductivity measurement is the same as the electronics of a wire-mesh tomograph [9] and is briefly described below. Figure 2a depicts the timing diagram for the excitation and measuring scheme and figure 2b presents the block diagram of the measuring electronics. The transmitter electrodes are connected to a bipolar voltage in a successive order while all the other transmitter electrodes are connected to ground potential by means of a set of analog switches. The outputs of the switches are buffered by operational amplifiers in order to create a low impedance path. This step assures that the potential of all transmitter electrodes, except the one of the actually activated electrode, are at ground potential. Furthermore, a bipolar voltage (dc-free) is employed to avoid electrolysis effects. The electrical currents flowing from the activated electrode to the sensing electrode is converted to voltage by a transimpedance amplifier. Typical wave forms for the excitation and the measured voltages are also shown in figure 2. All voltages are analog-to-digital converted simultaneously at the rising edge of the sample-and-hold signal. This routine is repeated for all transmitter electrodes being activated. Once all 64 transmitter electrodes have been activated and all currents have been measured, one frame is obtained containing 4096 values which corresponds to the distribution of the electrical conductivity over the sensor surface. The various frames acquired during a measurement are saved in a 64 × 64 × N_t data matrix in computer memory, where 64 is the

number of transmitter and receiver electrodes and N_t denotes the number of times steps. The electronics is able to produce up to 2500 images per second [10].

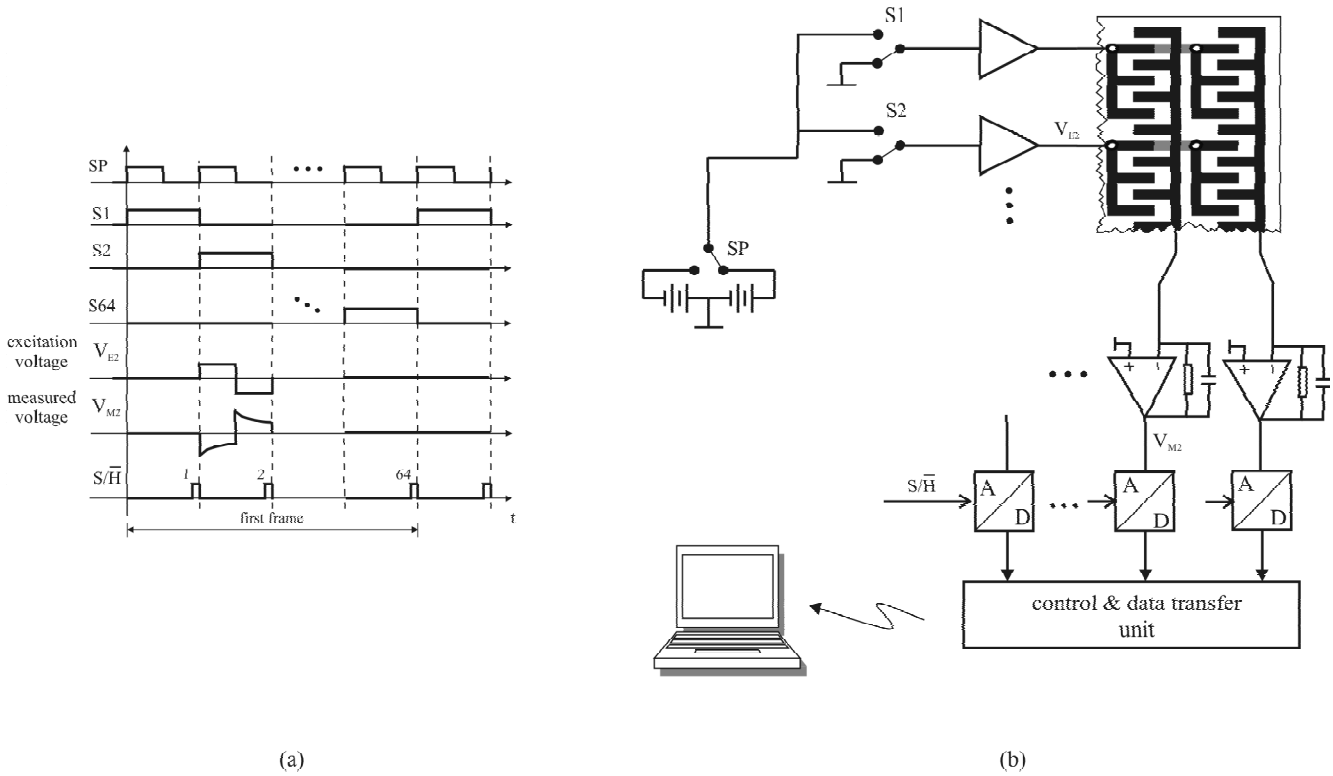

Figure 2. (a) Timing diagram for the multiplexed excitation and measuring scheme for the sensor. The signal SP denotes the polarity switch and S1 to S64 the analog switches. Voltages are sampled at the rising edge of the sample-and-hold signal. One frame is complete when the 64 transmitter electrodes have been activated and all currents have been measured. (b): Block diagram of the measuring electronics.

3. Interpreting the measured data

The voltage values measured by the surface sensor are proportional to the electrical current flowing from the transmitter electrode to the receiver electrode. This current basically depends on two parameters; the electrical conductivity κ of the liquid and the liquid wetting level of a sensing structure. Depending on the application one of those two parameters can be explored to generate information about the fluid distribution across the sensor. Since the system generates only one measurement for two unknowns, one of the parameters must be known or kept constant during the experiments to generate an unambiguous output. In this way, two different situations can be investigated. In the case the wetting level is constant, that means, the sensing structures are always covered by liquid, conductivity tracers can be applied to evaluate the flow in the channel. The other choice is to measure the liquid distribution across the sensor assuming the conductivity being constant. For instance, the presence of gas bubbles on the surface can be detected due to the fact the bubbles will change the wetting level of a sensing structure.

The acquired voltages for all sensing structures are saved in a data matrix in computer memory, in the form $V(i,j,k)$ where i and j denote spatial coordinates and k the temporal point index. In principle the evaluation of the measured voltage matrix $V(i,j,k)$ would be sufficient to investigate the component or phase distribution across the sensor. However, differences in the electrical response of the individual transmitter-receiver pairs, due to tolerances of electronic component or sensor elements, cause a variance in the measured signals which in turn produces artifacts in the resulting images. To compensate this variance two strategies are used to correct sensor's outputs depending on the measurement type, which are described bellow.

In the case, absolute conductivity values are to be assessed, the formula

$$\kappa(i,j,k) = V(i,j,k) \cdot a(i,j) + b(i,j) \tag{1}$$

may be used as correction relation, since the measured voltage is directly proportional to the electrical conductivity of the liquid over the sensing structure. The parameters $a(i,j)$ and $b(i,j)$ are determined from measurements at liquids with known conductivity. For this reason, data are firstly acquired with a substance of low conductivity κ^{L} covering the whole sensor, thus producing the reference data matrix $V^{L}(i,j)$. Normally average values over a certain time are used to reduce statistical signal fluctuations. This procedure is then repeated with the entire sensor surface covered with another substance having a higher conductivity value κ^{H}, which gives the second data matrix $V^{H}(i,j)$. In this fashion, applying (1) for both measurement situations, it is possible to determine them from

$$a(i,j) = \frac{\kappa^{H} - \kappa^{L}}{V^{H}(i,j) - V^{L}(i,j)}, \tag{2}$$

$$b(i,j) = \frac{V^{H}(i,j)\kappa^{L} - V^{L}(i,j)\kappa^{H}}{V^{H}(i,j) - V^{L}(i,j)}. \tag{3}$$

For the case that the wetting level or phase distributions are to be determined instead of conductivity values, we may introduce the parameter "wetting level" $w(i,j,k)$ which is determined from the ratio of the measured voltage and a reference point, i.e.

$$w(i,j,k) = \frac{V(i,j,k)}{C(i,j)}, \tag{4}$$

where $C(i,j)$ is the reference point which is obtained from a measurement when the whole sensor is covered by liquid. This way, the wetting level w assumes values between zero and one, meaning fully dry or fully wet sensing structure, respectively.

With the above described procedure images of the instantaneous fluid distributions across the sensor can be generated by mapping the wetting level $w(i,j,k)$ or conductivity values $\kappa(i,j,k)$ to a color

scale and then plotting them in the spatial directions of i and j for a fixed value of index k. Furthermore, sequences of these distributions can be viewed as video sequences by stepwise incrementing the temporal index k.

4. Sensor evaluation

4.1. Accuracy in electrical conductivity measurement

The primary output quantity of the planar sensor is an instantaneous image of the fluid distribution across the sensor surface. Based on these images some derived parameters may be obtained. Basically two applications fields may be identified for the planar sensor: applications that require only qualitative or morphological fluid distributions, e.g. for flow pattern identification, and applications that require quantitative evaluation of the fluid distribution, e.g. concentration measurement.

A complete metrological characterization of the output quantity as described by the GUM approach [11] requires the statistical evaluation of the intrinsic uncertainty of the measurand (multiphase or multicomponent flow in this paper) due to its transient nature, a rigorous description of the measurement process, and the identification of the more significant influence parameters. Therefore, different set of parameters are required to analyze the accuracy of quantities obtained from sensor measurements for each one of the two applications groups previously mentioned. Independent of application, image quality and accuracy of derived parameters depend on the accuracy of the electrical conductivity measurement.

In this fashion, instead of performing a rigorous uncertainty evaluation as suggested by GUM [11], the analysis in this section was limited to the evaluation of only two system characteristics which are related to electrical conductivity measurements. Thus, first the corrections proposed in section 3 are validated and second the instrumental noise in the electrical conductivity measurement is evaluated. These parameters solely represent the sources of uncertainty introduced by the proposed measurement apparatus itself. Further, the experiments presented here were carried out using difference solutions with known electrical conductivity values (working standard here), which are determined by a commercial conductivity meter Cond 330i (WTW GmbH, Germany, 0.5% accuracy).

For validating the correction procedure proposed in the previous section different concentrations of sodium chloride were dissolved in deionized water thus obtaining solutions with different electrical conductivity values. The flow channel of figure 1 was sequentially filled with water and NaCl solution having a known conductivity value. Reference conductivity of the samples was measured by the conductivity meter. For each reference conductivity value ten frames were acquired with the array sensor at a frequency of 2500 Hz and averaged to suppress random noise. Figure 3a depicts the measured voltage values in dependence of the reference conductivity for all 4096 sensing structures. The error bars represent the maximal inter-channel signal deviation from the mean values (circles). The three solid lines denote the linear fits for mean, maximal and minimal values within a same reference conductivity value. A linear dependence of V over κ is obtained, as anticipated by (1). Each driving-sensing electrode pair has its own response. The great inter-channel deviation is clearly shown in the plot. Its maximal value accounts to 32% when compared to the mean value. Basically 4096 lines with different slopes and constant terms are obtained. In this way, the need for a systematic error correction routine is evident, as already described in section 3. The results obtained after the correction

procedure are compared with the reference conductivity values in figure 3b. The error bars represent the maximal inter-channel signal deviation within a single conductivity value. The horizontal error bars associated with the reference conductivity measurements (0.5%) are too small to be visualized. The maximal value for the inter-channel deviation is reduced to 7%, excluding the measurement at 3 µS/cm (first data point in figures 3a and 3b). Furthermore, all measurements for conductivity values above 50 µS/cm fall within a 10% error boundary (dashed lines) from the ideal line (full lines). This value may be taken to represent the component of uncertainty in the electrical conductivity measurement due to systematic effects.

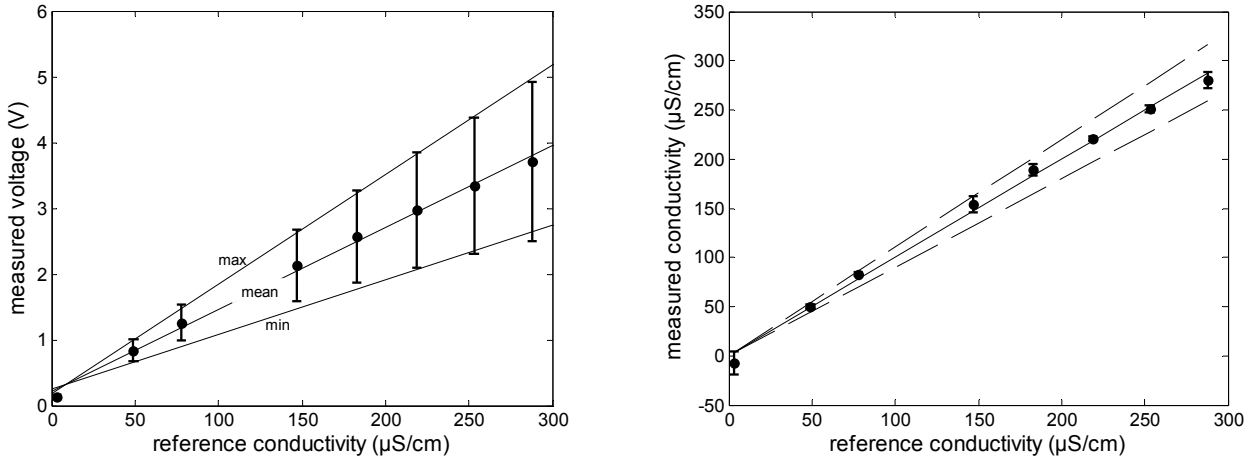

(a) (b)

Figure 3. (a) Measured voltage in dependence of the electrical conductivity. The three solid lines represent the linear fits for mean, maximal and minimal values within a same reference conductivity value. (b) Comparison of the measured κ from (1) after correction with reference values. The dashed lines represent the 10% deviation from the ideal line (solid line). In both plots the errors bars denote the maximal deviation from mean values (full circles). The horizontal error bars associated with the reference measurements (0.5%) are too small to be visualized.

To assess the level of instrumental noise the following procedure was used. First, 1000 frames at 2500 Hz were acquired from the flow channel filled with salt water solution at eight different reference conductivity values (same reference points as above). The values after equation (1) and the correction procedure were taken, thus the measured electrical conductivity values are being evaluated. Second, the standard deviation in the electrical conductivity value $\sigma_\kappa(i,j)$ for each sensing structure over the 1000 frames was determined. The relative noise level was defined as

$$n(i,j) = \frac{\sigma_\kappa(i,j)}{\kappa} \tag{5}$$

for each $i = 1\ldots64$ and $j = 1\ldots64$, where κ denotes the reference conductivity. The relative noise level was preferred instead of an absolute value in order to compare the values obtained for different signal levels. Figure 4a shows exemplary the histogram distribution of the relative noise level $n(i,j)$ of all 4096 sensing structures at a reference conductivity of 147 µS/cm. The maximal values among $n(i,j)$ for

all reference conductivities was plotted in figure 4b. Despite of the measurement at 3 µS/cm all obtained relative noise values are below 1%.

The measurements for the conductivity value of 3 µS/cm have a too low voltage level (mean value of 130 mV, see Fig. 3a), thus being more sensitive to noise and consequently lowering the accuracy of measurements. If lower conductivities values are to be investigated with the sensor, some parameters of the electronics such as amplifier gains or the excitation voltage level can be easily adapted for a new operation range.

According to GUM [11], when calculating the combined standard uncertainty, all uncertainty components are treated equally, no matter if they come from random or systematic effects. Assuming that the only sources of errors in the system are deriving from systematic effects (insufficient correction) and random noise, the relative combined standard uncertainty is obtained from the positive square root of the quadratic sum of both components (trivial propagation of uncertainty). However, since the uncertainty deriving from systematic effects (10%) is one order of magnitude higher than the above-mentioned noise level (1%), it is the dominant component and it may be used alone to represent the relative standard uncertainty in the electrical conductivity measurement in the range $\kappa \geq 50$ µS/cm.

It is worth to note that the measurements carried out here were performed at frame rates of 2500 fps. Even operating at a rather high frame rate the system presents good accuracy.

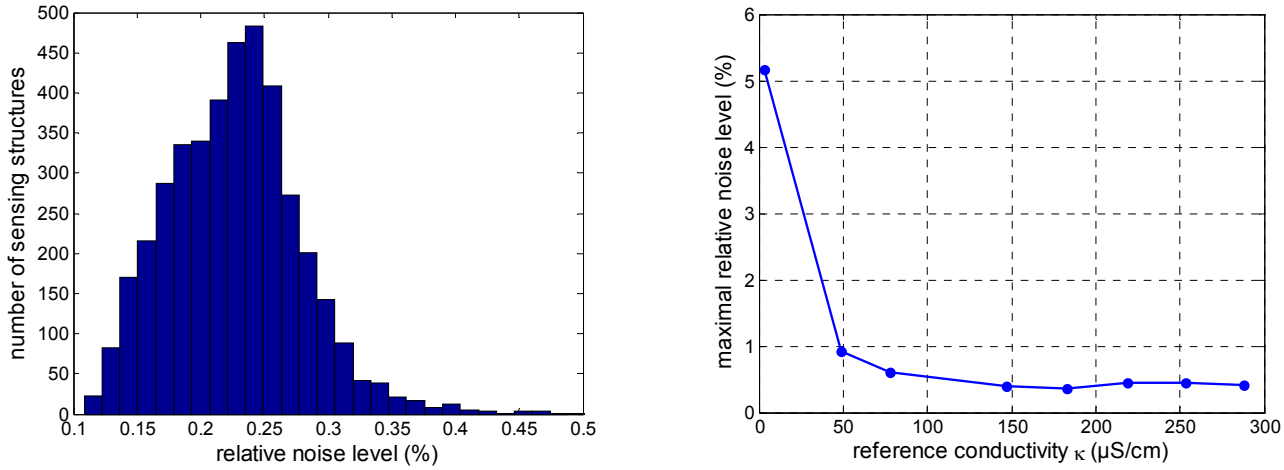

Figure 4. (a) Exemplary relative noise level distribution for a reference conductivity value of 147 µS/cm. (b) Maximal relative noise level for several reference conductivity values κ.

4.2. Depth sensitivity

In order to experimentally evaluate the depth sensitivity of the sensor, the following experiment was carried out. The flow channel of figure 1 with the integrated planar sensor was firstly put in the horizontal position. A glass plate of 120 mm × 200 mm size and 3 mm thickness was placed over the planar sensor so that one of its endpoints was raised by a thin plastic spacer of 1.5 mm thickness while the other one was in direct contact with the sensor, forming an inclined plane as shown in figure 5a.

The flow channel was then filled up with water (conductivity of 250 µS/cm). This way, a continuously growing water thickness over the sensor in an area of 15 × 25 sensing structures was generated. In the following analysis only this area was taken into account. Ten frames at 2500 fps were acquired and averaged. From the measured voltage values the wetting levels were computed from (4) and a reference measurement which was previously taken when the whole sensor was fully covered by water without plate. Figure 5b shows the mean values over the 15 rows for the calculated wetting levels. The form of the curve is an exponential rise which commensurate with previous analysis of interdigital structures [8]. There is no strict definition of penetration depth. Therefore we define the penetration depth γ of the sensor as the liquid thickness producing a signal level which represents 97 % of the asymptotic value ($w = 1$), i.e. the value for the case the thickness is infinite. This way,

$$\frac{V(z=\gamma)}{V(z=\infty)} = 0.97\,, \tag{6}$$

where z is the water thickness across the sensor. By using interpolation of the measured data, one obtains a value of $\gamma = 0.69$ mm. This value represents the maximal liquid thickness which influences the measurements at the planar sensor.

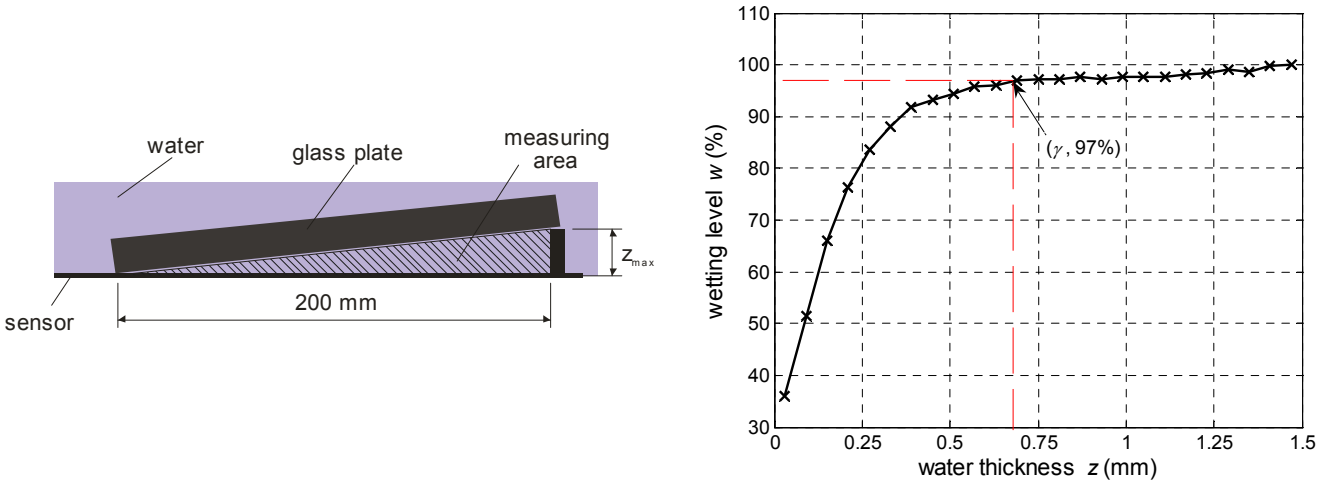

(a) (b)

Figure 5. (a) Experimental setup for the depth sensitivity estimation.
(b) Wetting level response for different water thickness over the sensor surface.

5. Flow measurement

To show the applicability of the new developed sensor to investigation of flow problems two selected flow experiments have been carried out which are presented and discussed in this section. It is not the aim here to completely investigate the flow phenomena, but rather present the sensor as new experimental tool.

5.1. Buoyancy-driven flow

Many fluid flows are driven by buoyancy, the tendency of hot fluid being less dense to rise, and cold fluid to sink. Buoyancy-driven flow is often present in engineering application, for instance the cooling of nuclear reactors and electronic components and the spread of pollutants through groundwater. Especially the problem of fluid mixing in nuclear reactors has been the scope of investigation of many researchers [12,13]. However, the influence of buoyancy is still not well understood in such scenarios regarding modeling and implementation in CFD due to the high complex geometry of the test facilities used, which are down-scale models of currently in use reactor vessels [14]. To investigate the phenomena involved with buoyancy a very simple test rig was designed and constructed which ensures that the gravity force acts along a significant length scale. To visualize the mixing process of two liquids having different densities in a controlled manner the following experiment was carried out. A schematic diagram of the test facility is shown in figure 6. It is 3.32 m high. Five identical rectangular segments as described in section 2 (Fig. 1) are attached together. The inlet is placed in between segments 1 and 2, while the outlet is positioned in between segments 4 and 5. Segment number 2, right after the inlet, is instrumented with the planar sensor. In this region the most interesting mixing process occurs.

Water-glucose mixtures were used to simulate density or temperature gradients. A glucose-water solution containing 6 % glucose has a corresponding density of 1020 kg·m^{-3} [13], i.e. 2 % density difference to clean water or about 60 K temperature difference. Furthermore, sodium chloride was added to the higher density water-glucose solution acting as tracer. This way, the mixing process of clean water with the glucose-water solution can be well monitored by means of the planar sensor evaluating (1). It has been shown that the conductivity measurement can be linked to the temperature or density gradients by [13,14]

$$\theta(i,j,k) = \frac{\kappa(i,j,k) - \kappa_{\mathrm{L}}}{\kappa_{\mathrm{H}} - \kappa_{\mathrm{L}}} \cong \frac{T(i,j,k) - T_{\mathrm{L}}}{T_{\mathrm{H}} - T_{\mathrm{L}}} \cong \frac{\rho(i,j,k) - \rho_{\mathrm{L}}}{\rho_{\mathrm{H}} - \rho_{\mathrm{L}}}, \tag{7}$$

where θ is called mixing scalar (assuming values between 0 and 1), κ is the measured conductivity, T is temperature and ρ is density. The subscripts H and L stand for the high and low values, respectively, which represent the parameter difference of the used liquids. In our experiment clean water had a conductivity of 60 µS/cm and the water-glucose solution 200 µS/cm.

The execution of the experiment consists of few subsequent steps. First clean water is added into the test section up to the bottom of segment 2. Second water-glucose solution is very slowly inserted from

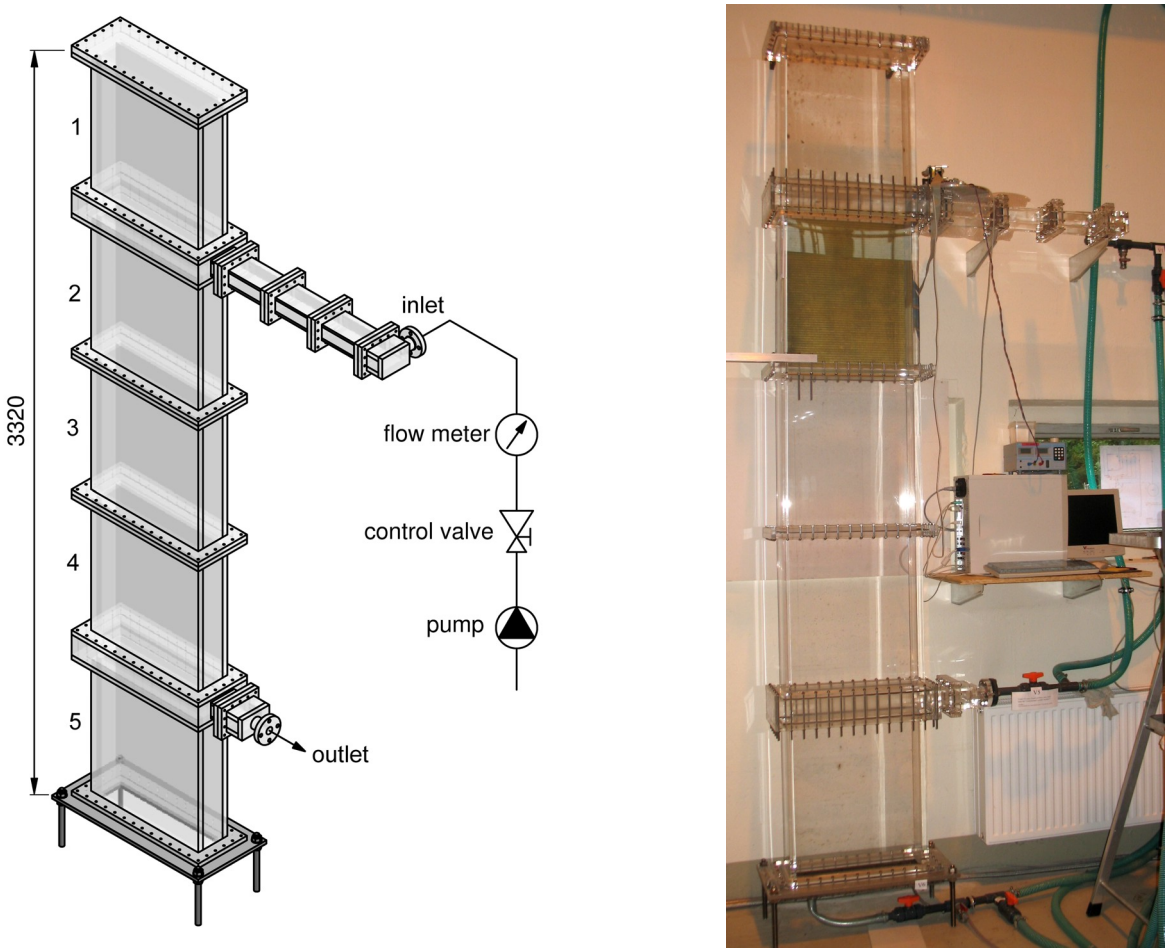

(a) (b)

Figure 6. Schematic diagram (a) and photograph (b) of the test facility used in the buoyancy-driven flow experiment.

the bottom taking the care not to mix the both components. This way, a layered structured is obtained having clean water in segments 1-2 and the more dense water-glucose solution in segments 3-5. This well-defined initial condition is very important for later comparison purposes with CFD simulations. Finally, the mixing process is initiated by flowing water-glucose solution through the inlet with a constant flow rate of 0.35 L/s. The process was monitored with the planar sensor for 200 s at 300 fps. Since the mixing process is rather slow the frame frequency could also be lowered. Figure 7 depicts twelve instantaneous mixing scalar θ distributions over the sensor surface. In the image for $t = 0$, the boundary between the two components as well as a transition region can be observed. It is very clear to see the formation of a circular jet, as the water-glucose solution flows into the channel. The time-resolved imaging of the process can reveal some details about the mixing behavior of two miscible liquids with different densities. In a later phase CFD simulations for different flow rates and density gradients will be validated with the experiments carried out with the planar sensor.

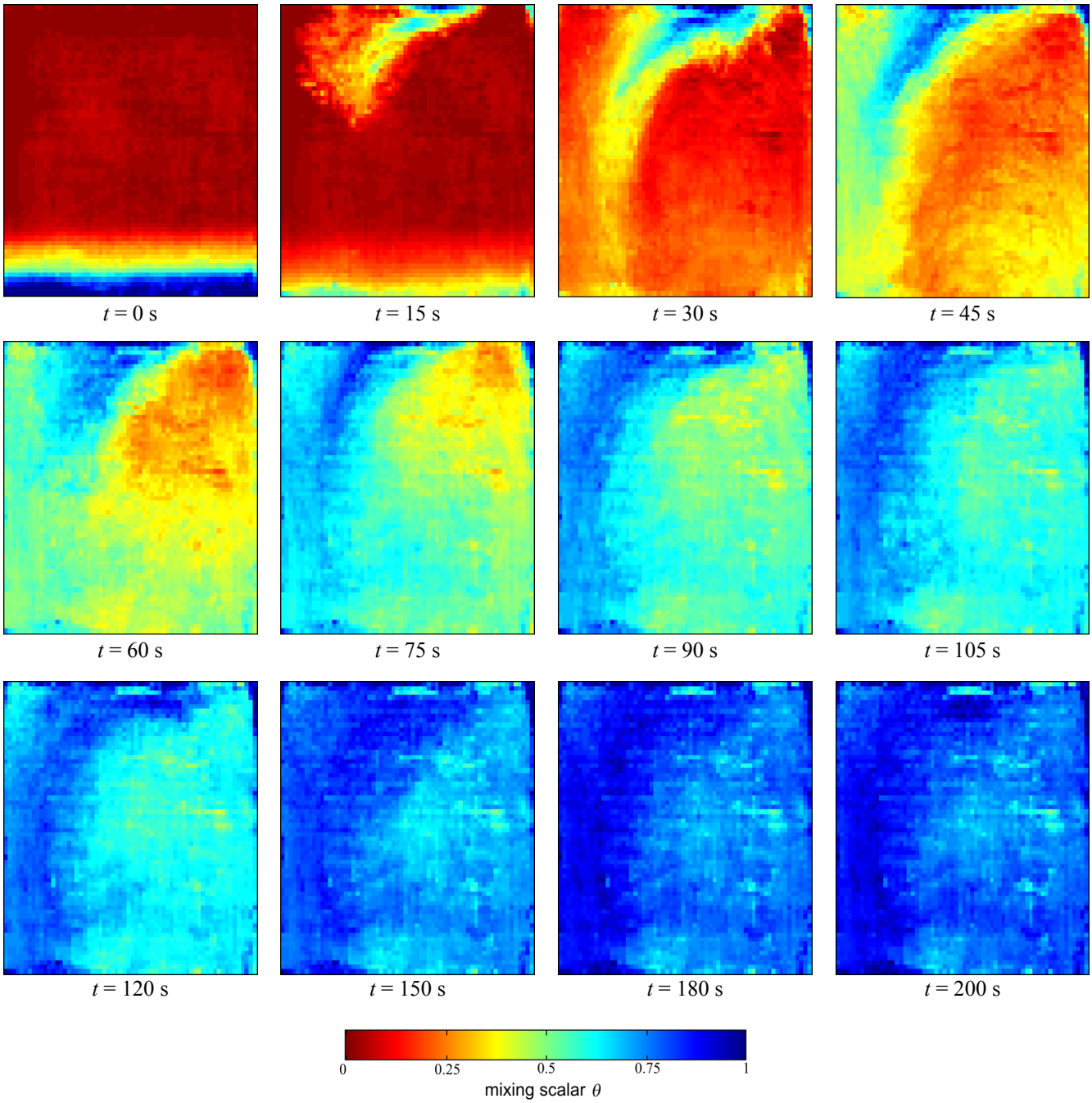

Figure 7. Instantaneous images of the mixing scalar θ. For details about the experiment see text.

5.2. Plunging jet

In several industrial applications mixing caused by a liquid jet impinging on a liquid surface is of interest. Depending on the jet velocity bubble entrainment may occur and influence the mixing. One example is the so-called Pressurized Thermal Shock (PTS) which is important for some accident scenarios of Pressurized Water Reactors (PWR). In these scenarios cold water is injected into a PWR cold leg partially filled with hot water and with steam. Turbulence generated by the jet and bubble entrainment influence the mixing of the hot and cold water. The mixing is important to limit thermal loads at the hot Reactor Pressure Vessel walls [15]. There are ongoing activities to simulate the

plunging jet flow situation using CFD codes [16]. The process of bubble entrainment is very complex and additional models are required. The jet causes a deformation of the surface appearing as an annular meniscus. Instabilities at the lower part of this meniscus generate bubbles (see Fig. 8). Experimental data are required on the shape of the annular meniscus, on the entrained gas volume flow rate, the sizes of the generated bubbles, the entrainment depth, local gas volume fraction distributions and on velocity fields of gas and liquid below the jet. CFD model development and validation require such data with high resolution in space and time.

Up to now the experimental investigation of plunging jet problems has been basically performed by optical methods (high-speed videometry, PIV, PLIF), local void fraction probes or acoustic methods [17-19]. However, each one of those methods has some limitation. For instance, optical methods are only reliable for low gas fraction, the local probes besides being invasive (may disturb the flow) provide only localized data and finally acoustic methods supply only averaged data without spatial information. In addition, hitherto all methods have almost exclusively been applied for normal environmental conditions, i.e. low temperature, low pressure. The new developed array sensor can be used in situations where other methods might fail, i.e. high gas fraction, harsh environmental conditions or where spatial information is desired, thus complementing the lack of information in the dynamics of plunging jets.

A simple plunging jet experiment was realized to show the capability of sensor in investigating such problems. The flow channel of fig. 1 was filled with water (κ = 200 µS/cm) up to 200 mm below the top level. A water circular jet of 5 mm diameter and flow rate of 0.1 L/s was generated and plunged into the flow channel at an angle of 90°. This experiment was carried out twice, once with water having the same conductivity value as the water in the flow channel and a second time with a less conductive water (κ = 50 µS/cm). Data were acquired with 2500 fps.

Exemplary images of the measurement for both situations can be seen in figure 9. In the first measurement the images were generated using (4), whereas single bubbles can be detected (fig. 9a). For the second experiment the use of the tracer enables the investigation of the mixing process in the liquid phase (fig. 9b) by evaluating (1), after correction procedure. The bubbles generated are hidden by the tracer. Hence both experiments complement each other. By the first experiment the dynamic of bubbles and the process of bubble entrainment can be investigated while by the second one the liquid phase and the mixing process are studied. Some information can be directly obtained from the images for instance the depth penetration of the jet or the bubbly flow below the jet. Furthermore, the interpretation of data obtained still has to be clarified because of the interaction between the bubbles and the sensor. Also a sensor with finer spatial resolution than the one used here could possibly supply information on the annular meniscus and on bubble generation and will be investigated in the future.

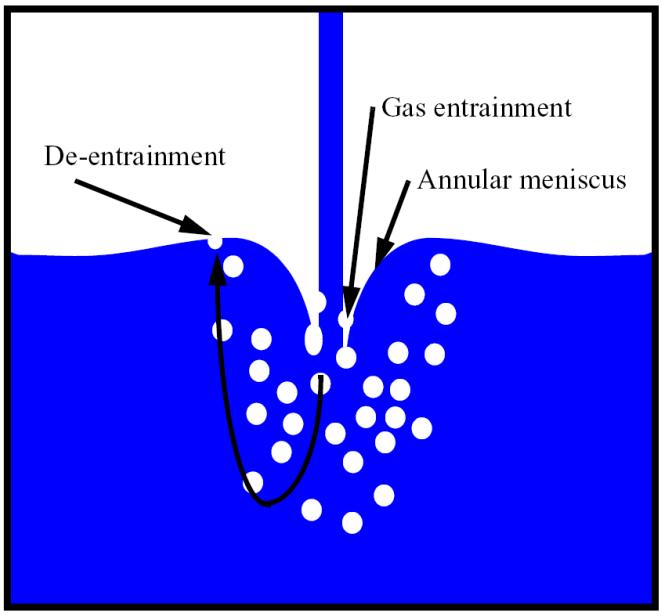

Figure 8. Gas entrainment caused by a plunging jet

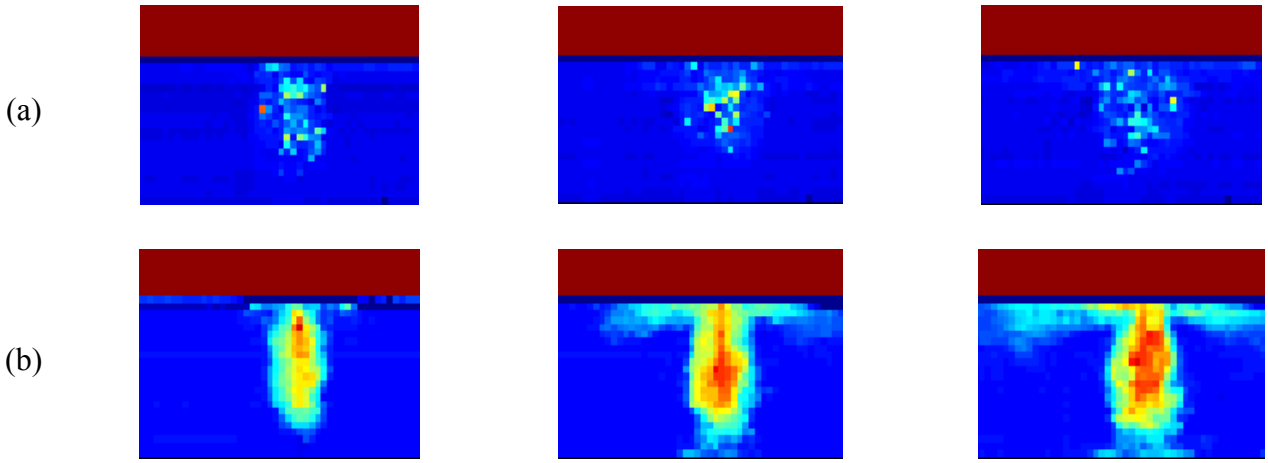

Figure 9. Results of a simple plunging jet experiment. (a) Bubble detection experiment and (b) mixing process experiment. For simplicity the images were cropped to the region of interest.

5. Conclusions

A new tool for the investigation of fluid flow phenomena has been developed and tested. The planar sensor is able to detect phases or components in dynamic fluid flow. The electronics performs a two-dimensional measurement of electrical conductivity at the sensor surface, which effectively gives images of the instantaneous fluid distribution over the sensor surface. The system's high-speed capability enables its application in the investigation of highly transient flows. We have employed the sensor in two different flow problems, namely, buoyancy-driven flow and plunging jet experiments. Future work will encompass improved analysis of the data acquired in the plunging jet experiment and the deployment of the sensor for the investigation of further flow problems. The simplicity and low

cost of the standard PCB fabrication technology permits a rapid design and manufacturing of arbitrary sensor geometries which may be required for other applications.

Acknowledgements

The first author acknowledges the Brazilian agency CAPES ("Coordenação de Aperfeiçoamento de Pessoal de Nível Superior") for the financial support by a doctoral grant.

References and Notes

1. Mamishev, A.V.; Sundara-Rajan, K.; Yang, F.; Du, Y.; Zahn, M. Interdigital sensors and transducers. *Proceedings of the IEEE* **2004**, *92*, 808-845.
2. Mukhopadhyay, S. C. Novel Planar Electromagnetic Sensors: Modeling and Performance Evaluation. *Sensors* **2005**, *5*, 546-579.
3. Kaatze, U.; Feldman, Y. Broadband dielectric spectrometry of liquids and biosystems. *Measurement Science and Technology* **2006**, *17*, R17-R35.
4. Wittstock G. Sensor arrays and array sensors. *Analytical and Bioanalytical Chemistry* **2002**, 372, 16-17.
5. Gardner, J.W.; Pike, A.; de Rooij, N. F.; Koudelka-Hep, M.; Clerc, P.A.; Hierlemann, A; Opel, W.G. Integrated array sensor for detecting organic solvents. *Sensors and Actuators B* **1995**, *26-27*, 135–139.
6. Hermes, T.; Bühner, M.; Bücher, S.; Sundermeier, C.; Dumschat, C.; Borchardt, M.; Cammann, K.; Knoll, M. An amperometric microsensor array with 1024 individually addressable elements for two-dimensional concentration mapping. *Sensors and Actuators B* **1994**, *21*, 33-37.
7. Wang, H.X.; Yin, W.; Yang, W.Q.; Beck, M.S. Optimum design of segmented capacitance sensing array for multi-phase interface measurement. *Measurement Science and Technology* **1996**, *7*, 79-86.
8. Li, X.B.; Larson, S.D.; Zyuzin, A.S.; Mamishev, A.V. Design Principles for Multichannel Fringing Electric Field Sensors. *IEEE Sensors* **2006**, *6*, 434-440.
9. Prasser, H.M.; Böttger, A.; Zschau, J. A New Electrode-Mesh Tomograph for Gas-Liquid Flows. *Flow Measurement and Instrumentation* **1998**, *9*, 111-119.
10. Prasser, H.M.; Zschau, J.; Peters, D.; Pietzsch, G.; Taubert, W.; Trepte, M. Fast wire-mesh sensors for gas-liquid flows – Visualization with up to 10,000 frames per second. In *Proceedings of ICAPP*, Hollywood, Florida, 2002; Paper No. 1055.
11. ISO Guide to the expression of uncertainty in measurement (GUM); ISO Publishing, 1995.
12. Rohde, U.; Kliem, S.; Höhne, T.; Karlsson, R.; Hemström, B.; Lillington, J.; Toppila, T.; Elter, J.; Bezrukov, Y. Fluid mixing and flow distribution in the reactor circuit, measurement data base. *Nuclear Engineering and Design* **2005** *235*, 421-443
13. Prasser, H.-M.; Grunwald, G.; Höhne, T.; Kliem, S.; Rohde, U.; Weiss, F.-P. Coolant mixing in a pressurized water reactor: deboration transients, steam-line breaks, and emergency core cooling injection. *Nuclear Technology* **2003**, *143*, 37-56.

14. Höhne, T.; Kliem, S.; Bieder, U. Modeling of a buoyancy-driven flow experiment at the ROCOM test facility using the CFD-codes CFX-5 and TRIO_U. *Nuclear Engineering and Design* **2006**, *12*, 1309-1325.
15. Lucas, D.; Bestion, D.; Bodèle, E.; Scheuerer, M.; F. D'Auria, D. Mazzini; Smith, B.; Tiselj, I.; Martin, A.; Lakehal, D.; Seynhaeve, J.-M.; Kyrki-Rajamäki, R.; Ilvonen, M.; Macek, J. On the simulation of two-phase flow pressurized thermal shock (PTS). In: *12th International Topical Meeting on Nuclear Reactor Thermal Hydraulics (NURETH-12)*, Pittsburgh, Pennsylvania, U.S.A. , Sept 30 - Oct 4, 2007; Paper No. 035.
16. Lucas, D., Ed., Review Identification of relevant PTS-scenarios, state of the art of modeling and needs for model improvements, *6th Euratom Framework Program NURESIM*, Deliverable D2.1.1, 2005. Available at: http://www.nuresim.com/Documents/Document%20Library/SP2%20-%20Thermalhydraulics/Reports/D2.1.1_final.pdf.
17. Reungoat, D.; Riviere, N.; Faure J.P., 3C PIV and PLIF measurement in turbulent mixing - Round jet impingement. *Journal of Visualization* **2007**, *10*, 99-110.
18. Bonetto, F.; Lahey Jr, R.T., An experimental study on air carry-under due to a plunging liquid jet. *International Journal of Multiphase Flow* **1993**, *19*, 281 – 294.
19. Chanson, H,; Manasseh, R. Air Entrainment Processes in a Circular Plunging Jet: Void-Fraction and Acoustic Measurements. *Journal of Fluids Engineering* **2003**, *125*, 910-921.